ENVIRONMENTAL ENGINEERING SCIENCE
Volume 38, Number 3, 2021

DOI: 10.1089/ees.2020.0369

Sealing Porous Media through Calcium Silicate Reactions with CO_2 to Enhance the Security of Geologic Carbon Sequestration

Florence T. Ling,[1,2,*] Dan A. Plattenberger,[3] Catherine A. Peters,[2,†] and Andres F. Clarens[3,†]

[1]*Environmental Science Program, Department of Chemistry and Biochemistry, La Salle University, Philadelphia, Pennsylvania, USA.*
[2]*Civil and Environmental Engineering, Princeton University, Princeton, New Jersey, USA.*
[3]*Engineering Systems and Environment, University of Virginia, Charlottesville, Virginia, USA.*

Received: September 2, 2020 *Accepted in revised form: December 31, 2020*

Abstract

The injection of CO_2 deep underground, i.e., geologic carbon sequestration, has attracted considerable attention for climate change mitigation. A reliable caprock for secure containment is essential, alongside strategies for sealing flow paths to prevent leaks. In this study, we explore ways in which reactions of CO_2 with $CaSiO_3$ can be used for targeted mineral precipitation and permeability control *in situ*. Previous work has suggested that certain $CaSiO_3$ polymorphs can produce pore-filling precipitates that successfully inhibit flow, whereas others produce precipitates with little impact. In this work, a one-dimensional reactive transport model was developed for a centimeter-scale system to explore connections between the pore and continuum scale. The model considers four reactions involving $CaSiO_3$, $CaCO_3$, $SiO_{2(am)}$, and the crystalline calcium silicate hydrate (CCSH) tobermorite. A key feature is incorporation of microporosity, with an attempt to represent favorable volume expanding changes from CCSH precipitation in porous media. At 150°C and 1.1 MPa CO_2, representing typical laboratory conditions, the model predicts significant permeability drop when reacting the pseudowollastonite $CaSiO_3$ polymorph at elevated pH to produce $CaCO_3$, $SiO_{2(am)}$, and tobermorite. The effect of increasing pH via by NaOH addition, which increases CO_2 solubility, increases $CaSiO_3$ dissolution, and supports tobermorite supersaturation. In contrast, reaction of the wollastonite polymorph results in $CaCO_3$ and $SiO_{2(am)}$ formation, with limited permeability impact. Wollastonite's lower solubility and slower dissolution rate inhibits tobermorite formation. Simulation at the high pressures representative of deep subsurface field conditions (40°C and 7.5 MPa CO_2) suggests that reaction of $CaSiO_3$ with CO_2 could reduce permeability and seal unwanted leakage pathways.

Keywords: calcium silicate, CO_2, permeability, pseudowollastonite, reactive transport

Introduction

A GROWING INTEREST in deep subsurface environments for their importance in geologic CO_2 storage has resulted in concerns regarding the migration of fluids into the environment (White *et al.*, 2020). Sites of undesired fluid migration underground may include natural faults, fractures, or degraded areas associated with wellbores (Deng and Peters, 2019, 2020; Spokas *et al.*, 2019). In geologic sequestration of CO_2 deep underground, buoyant forces could allow CO_2 to leak from its storage location and escape into the atmosphere, undermining the goal of permanently sequestering CO_2 (Bohnhoff and Zoback, 2010; Bielicki *et al.*, 2015, 2016; Deng *et al.*, 2017). These risks highlight the need for approaches to seal leaks and control permeability and flow in the subsurface.

One possible solution for altering fluid flow in geologic CO_2 reservoirs is through controlled mineral precipitation by the targeted delivery of calcium silicates. The topic of carbon mineralization by silicate dissolution with subsequent precipitation of carbonate minerals has been well studied and that research has provided valuable insights about the controlling mechanisms of these geochemical reactions (Jun *et al.*, 2013; Zhao *et al.*, 2013; Stack *et al.*, 2014). However, these reactions have only recently been proposed in the context of subsurface technologies in support of induced precipitation for permeability control (Deng and Peters, 2019, 2020; Spokas *et al.*, 2019). Our recent work has examined the feasibility of such targeted mineral precipitation by delivering calcium silicate particles headed for leakage sites to produce secondary minerals that occupy pore space and decrease permeability (Fig. 1) (Tao *et al.*, 2016; Plattenberger *et al.*, 2019, 2020). Physical properties of the particles, including size, microporosity, and the use of polymer coatings (Lee *et al.*, 2007; Plattenberger *et al.*, 2020), can be engineered to

**Corresponding author:* Environmental Science Program, Department of Chemistry and Biochemistry, La Salle University, 1900 W. Olney Avenue, Philadelphia, PA 19141, USA. *Phone:* 215-951-1848; *Fax:* 215-951-1359; *E-mail:* ling@lasalle.edu
†Member of AEESP.

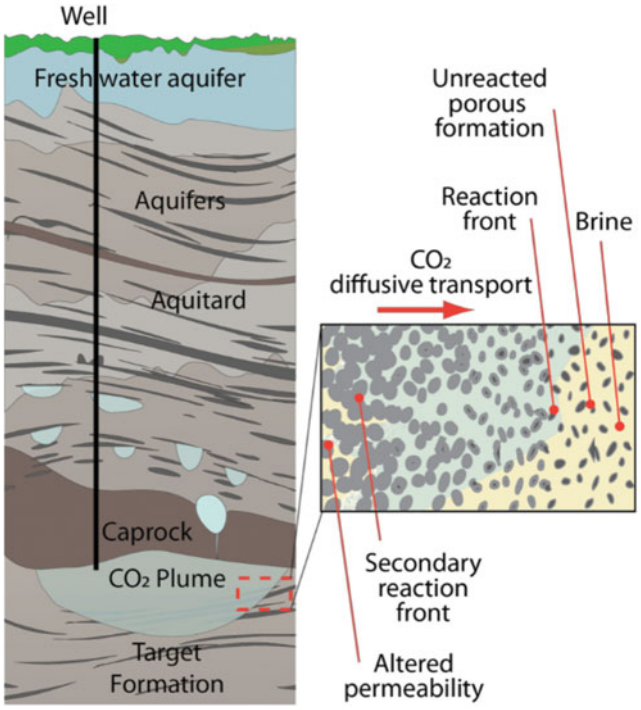

FIG. 1. A CO_2 plume from a target formation can potentially be sealed using targeted delivery of calcium silicate particles. The $CaSiO_3$ particles would react with the diffusing CO_2, producing mineral precipitates to decrease permeability, sealing the leakage.

control buoyancy, the extent of vertical migration during injection, and the temperature at which the reactions begin.

When considering $CaSiO_3$ reactions with CO_2, the mineral wollastonite has been widely studied for its ability to mineralize CO_2 into $CaCO_3$, while also forming $SiO_{2(am)}$ and minor amounts of crystalline calcium silicate hydrate (CCSH) (Berner *et al.*, 1983; Daval *et al.*, 2009b).

In contrast, the $CaSiO_3$ polymorph pseudowollastonite produces relatively larger quantities of CCSH when reacting with CO_2 (Ashraf and Olek, 2016; Plattenberger *et al.*, 2018, 2019; Monasterio-Guillot *et al.*, 2019). These differences may be due to pseudowollastonite's stoichiometric dissolution and wollastonite's nonstoichiometric dissolution (Casey *et al.*, 1993; Schott *et al.*, 2012). The difference in release rates of Ca^{2+} and $SiO_{2(aq)}$ is thought to affect whether $CaCO_3$ or CCSH forms (Plattenberger *et al.*, 2018; Monasterio-Guillot *et al.*, 2019).

The resulting CCSH phases exhibit properties that will likely benefit the development of targeted mineral precipitation technology for permeability control. CCSH phases show substantial resilience to redissolution in acid compared to $CaCO_3$ (Plattenberger *et al.*, 2018, 2019), a desirable characteristic to ensure the long-term containment of CO_2, which exists in aqueous solution as carbonic acid. Furthermore, the molar volumes of $CaCO_3$ (3.12×10^{-5} m^3) and $CaSiO_3$ (3.98×10^{-5} m^3) are quite similar and may not be advantageous for sealing subsurface leakages. We suspect that the large molar volumes of CCSH in comparison to $CaCO_3$ minerals, the ability of some CCSHs to expand and hold structural water, and the extensive microporosity observed in their formation will contribute to the pore-filling effectiveness of CCSH in porous media.

In this study, we used reactive transport modeling to explore calcium silicates in porous media reacting with diffusing CO_2 and the extent of permeability reduction due to mineral precipitation. The modeling was aimed at addressing the following questions: Why does dissolution of different calcium silicates, wollastonite and pseudowollastonite, affect mineral formation? How do the properties of CCSH, their ability to create microporosity, and their co-occurrence with $CaCO_3$ and $SiO_{2(am)}$ affect their ability to fill pore space? What pH conditions promote CCSH formation? Finally, how might changes in temperature and CO_2 pressure affect the reactions involved, particularly under field conditions for geologic CO_2 storage?

A one-dimensional (1D) reactive transport model was built to examine the conditions that allow for CCSH formation and quantify permeability alteration. Permeability was used as a metric to gauge the effectiveness of sealing the porous medium. For calibration of mineral precipitation kinetics and for model validation, simulations were compared with previously published experimental results in Plattenberger *et al.* (2019). In addition to the modeling, a single new experiment with a glass bead column was conducted, in which the column was filled with pseudowollastonite and reacted with CO_2. The column was examined using x-ray computed tomography (xCT) imaging to observe pore space filling and changes in pore connectivity.

One-Dimensional Reactive Transport Model

Model system

The model system was selected to represent a porous medium with nonadvective diffusive flux at one end, similar to that originally configured by Giammar *et al.* (2014). A diffusion-limited environment is expected at the edge of the CO_2 plume in a target formation (Fig. 1). A schematic of the model system is shown in Fig. 2. The constant boundary condition is represented as H_2O equilibrated with an overhead pressure of CO_2. Throughout this article, this boundary is referred to as the ''CO_2 source.'' The remainder of the cells represents the porous medium, initially containing $CaSiO_3$ and equilibrated with pH 7 solution. The last cell is a no-flux boundary. The cross-sectional dimensions of the 1D system were selected to allow comparison to experiments reported in Plattenberger *et al.* (2019) and cell volume calculations with changing porosity.

Reactions and rate laws

$CaSiO_3$ dissolution. $CaSiO_3$ dissolution and precipitation were modeled kinetically for both wollastonite and pseudowollastonite according to the following reaction:

$$CaSiO_3 + 2H^+ \leftrightarrow Ca^{2+} + SiO_{2(aq)} + H_2O \quad (1)$$

The rate of dissolution for wollastonite is described by the rate law derived from transition state theory:

$$r_{D,\,CaSiO3} = A\, k_{D,\,CaSiO3} \exp\left(-\frac{E_a}{RT}\right) a_H^n (1-\Omega_{CaSiO3}) \quad (2)$$

where the rate is in units of mol/s, A is the reactive surface area, $k_{D,\,CaSiO3}$ is the rate constant, E_a is the activation energy,

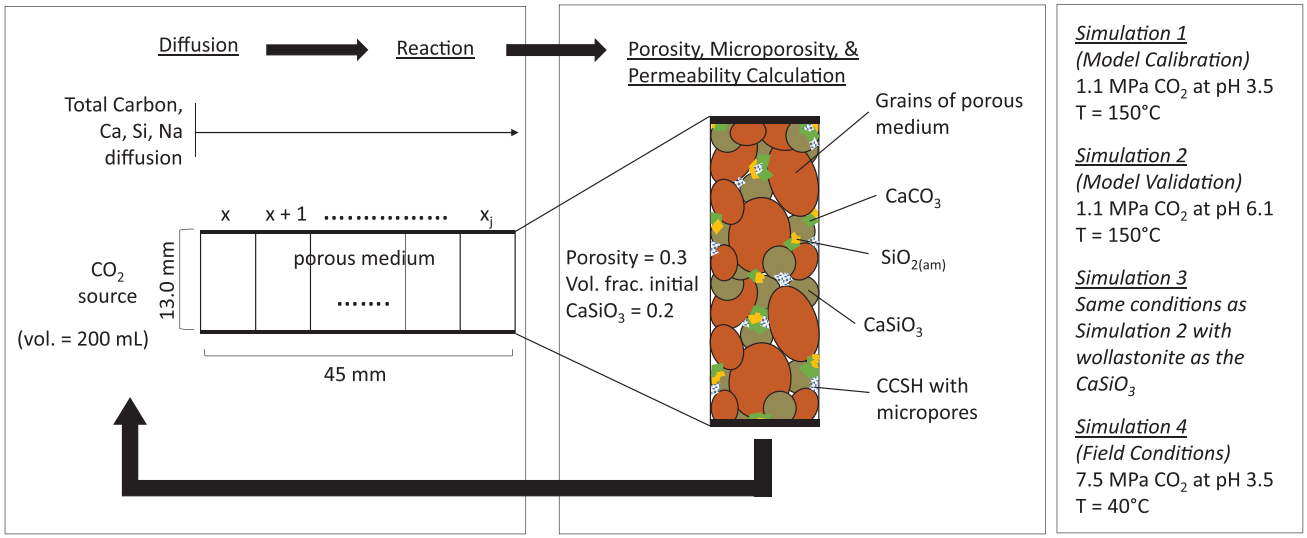

FIG. 2. Schematic summarizing the components of the one-dimensional model and the simulation conditions. The parameter x_j represents the space step, ranging from 0 to 45 mm.

R is the gas constant, T is temperature, a_H is the activity of H^+, and n is an exponent that quantifies the pH dependence of dissolution kinetics. The ratio of the ion activity product to the solubility constant for mineral i is Ω_i. For $CaSiO_3$,

$$\Omega_{CaSiO3} = \frac{\{Ca^{2+}\}\{SiO_{2(aq)}\}}{\{H^+\}^2 K_{sp,\,CaSiO3}} \tag{3}$$

For wollastonite, kinetic rate parameter values were estimated from Casey *et al.* (1993), Schott *et al.* (2012), and Ptáček *et al.* (2011), giving $k_{D,\,CaSiO3} = 10^{-1.30}$ mol/[cm^2·s], $E_a = 47$ kJ/mol, and $n = 0.31$. For pseudowollastonite, the dissolution rate constant of wollastonite was multiplied by $10^{2.16}$ to represent the higher dissolution rate of pseudowollastonite in comparison to the average of the wollastonite dissolution rates (Casey *et al.*, 1993). Dissolution was modeled as occurring when the saturation index (SI_i) of mineral i was less than 0. SI_i is expressed generally for all solids as follows:

$$SI_i = \log\Omega_i \tag{4}$$

All reaction parameters are included in Table 1.

$CaCO_3$ dissolution. The dissolution of $CaCO_3$ was modeled with the three parallel reactions:

$$CaCO_{3(s)} + H^+ \leftrightarrow Ca^{2+} + HCO_3^- \tag{5}$$

$$CaCO_{3(s)} + H_2CO_3^* \leftrightarrow Ca^{2+} + 2HCO_3^- \tag{6}$$

$$CaCO_{3(s)} \leftrightarrow Ca^{2+} + CO_3^{2-} \tag{7}$$

The dissolution of $CaCO_3$ follows the rate law (Plummer *et al.*, 1978; Chou *et al.*, 1989):

$$r_{D,\,CaCO3} = A(k_{D,\,C1} + k_{D,\,C2} + k_{D,\,C3})(1 - \Omega_{CaCO3}) \tag{8}$$

where $k_{D,\,C1}$, $k_{D,\,C2}$, and $k_{D,\,C3}$ (mol/[m^2·s]) are empirical temperature dependent rate parameters, T is the temperature (Kelvin), and A is the reactive surface area (m^2):

$$\log k_{D,\,C1} = 0.198 - \frac{444}{T} \tag{9}$$

$$\log k_{D,\,C2} = 2.94 - \frac{2177}{T} \tag{10}$$

$$\log k_{D,\,C3} = -1.10 - \frac{1737}{T} \tag{11}$$

$CaCO_3$ dissolves when the solution is undersaturated ($SI_{CaCO3} < 0$). Because Plattenberger *et al.* (2018) showed that wollastonite and pseudowollastonite reacted with CO_2 to produce calcite and aragonite, respectively, for wollastonite simulations, the solubility constant of calcite was used, while for pseudowollastonite simulations, the solubility constant of aragonite was used (Table 1).

$SiO_{2(am)}$ dissolution. The dissolution of amorphous silica was modeled based on the experimental results of others that observed $SiO_{2(am)}$ formation in the reaction of calcium silicates with CO_2 (Daval *et al.*, 2009a; Plattenberger *et al.*, 2018; Monasterio-Guillot *et al.*, 2019). Dissolution was modeled according to the following reaction:

$$SiO_{2(aq)} \leftrightarrow SiO_{2(am)} \tag{12}$$

When the solution was undersaturated with respect to $SiO_{2(am)}$, then dissolution was allowed to occur. The rate of dissolution, according to Dove and Crerar (1990), is as follows:

$$r_{D,\,SiO2(am)} = k_{D,\,SiO2} a_{SiO2(aq)} a_H^2 \left(1 - \Omega_{SiO2(am)}\right) \tag{13}$$

TABLE 1. MODELED REACTIONS AND KINETIC AND THERMODYNAMIC PARAMETERS

Dissolution and precipitation reactions

Reaction	*ΔH (kJ/mol)*	*$logK_{sp}$ (25°C)*	*$logK_{sp}$ (40°C)*	*$logK_{sp}$ (150°C)*	*Kinetics modeled*	*Source*	*V_m (m^3/mol)**	*V_m source*	*Specific Surface Area(m^2/g)*	*Dissolution rate constant $k_{D,i}$ (mol/[$cm^2 \cdot s$])*	*Calibrated $k_{P,i}$*
$CaSiO_{3(s)} + 2H^+ \leftrightarrow Ca^{2+} + SiO_2 + H_2O$	Woll: −76.5756	13.428	12.78	9.012	Dissolution and precipitation	SOLTHERM	3.98×10^{-5}	SOLTHERM	1.38	$10^{-1.30}$	3.98×10^{-13}
	Pseudo: −79.4625	14.169	13.47	9.456	Dissolution and precipitation	SOLTHERM	3.98×10^{-5}	SOLTHERM	1.38	$10^{0.86}$	
$SiO_{2(aq)} \leftrightarrow SiO_{2(am)}$	20.0539	−2.464	−2.37	−1.925	Dissolution and precipitation	SOLTHERM	2.90×10^{-5}	SOLTHERM	0.21	$10^{-9.9}$	1.00×10^{-2}
$Ca^{2+} + CO_3^{2-} \leftrightarrow CaCO_{3(s)}$	Calc: −9.61	−8.48	−8.56	−8.98	Dissolution and precipitation	PHREEQC LLNL	3.12×10^{-5}	SOLTHERM	0.21	N/A	1.32×10^{-6}
	Arag: −10.83	−8.336	−8.427	−8.897	Dissolution and precipitation	SOLTHERM	$3.42\times10-5$	SOLTHERM	0.21		1.32×10^{-6}
$Ca_5Si_6H_{11}O_{22.5(s)} + 10H^+ \leftrightarrow 5Ca^{2+} + 6SiO_{2(aq)}$	−286.9	65.6121	63.2	50.75	Equilibrium only	PHREEQC LLNL	2.83×10^{-4}	MINCRYST	N/A	N/A	

Aqueous speciation reactions

Reaction	*ΔH (kJ/mol)*	*$logK_{sp}$ (25°C)*	*$logK_{sp}$ (40°C)*	*$logK_{sp}$ (150°C)*	*Source*
$H_2CO_3 \leftrightarrow H^+ + HCO_3^-$	9.7	−6.347	−6.26	−5.84	Phreeqc LLNL database
$HCO_3^- \leftrightarrow H^+ + CO_3^{2-}$	−14.9	−10.33	−10.45	−11.1	Phreeqc LLNL database
$H_2O \leftrightarrow H^+ + OH^-$	55.91	−14	−13.53	−11.104	Phreeqc LLNL database

*The molar volume for each reaction is the molar volume of the solid phase in that reaction.

The rate constant $k_{D,SiO2}$ was calculated using the Arrhenius expression from Icenhower and Dove (2000). For $SiO_{2(am)}$,

$$\Omega_{SiO2(am)} = \frac{\{SiO_{2(aq)}\}}{K_{sp,SiO2(am)}} \quad (14)$$

Modeling of $CaSiO_3$, $CaCO_3$, and $SiO_{2(am)}$ precipitation. Precipitation reactions for $CaSiO_3$, $CaCO_3$, and $SiO_{2(am)}$, as described in Table 1, were modeled kinetically with rate equations. For all solids, precipitation was allowed to occur when the $SI_i > 0$, and according to the rate law (Kim *et al.*, 2011):

$$r_{P,i} = A\, k_{P,i}(1 - \Omega_i) \quad (15)$$

where the rate is in units of mol/[$cm^2 \cdot s$] and A is the reactive surface area. The precipitation rate constant, $k_{P,i}$, accounts for both the rate of precipitation and the energy barrier needed to overcome nucleation for solid phase i. It is difficult to define a $k_{P,i}$ value from the literature, because metastable aqueous solutions do not nucleate immediately upon oversaturation and can exist as an oversaturated solution over a wide range of saturation values differing by several orders of magnitude of Ω_i (Prieto *et al.*, 1994). In this study, values of $k_{P,i}$ (Table 1) were chosen by calibration to the sand column experiment reacting pseudowollastonite at 150°C with 1.1 MPa CO_2 described in Plattenberger *et al.* (2019). The details are discussed in the Model Calibration section. In addition, because the rate of precipitation is proportional to reactive surface area, when no initial precipitate was present, an artificial ''seed'' of 1×10^{-11} g was added to initiate precipitation. Chosen specific surface areas used to calculate reactive surface area based on the amount of this mineral phase are included in Table 1, although specific surface areas are known to vary widely.

CCSH dissolution and precipitation. CCSH dissolution and precipitation were modeled thermodynamically with no kinetic equations with tobermorite as the model CCSH. Tobermorite was chosen from many known CCSH phases because it is one of the most well-studied calcium silicate hydrates. In addition, Daval *et al.* (2009b) studied the reaction of wollastonite with CO_2 and identified small amounts of calcium silicate hydrate that was likely 14 Å-tobermorite. Monasterio-Guillot *et al.* (2019) also identified what was likely metastable tobermorite in pseudowollastonite carbonation reactions.

The dissolution reaction of 11 Å-tobermorite is described as follows:

$$Ca_5Si_6H_{11}O_{22.5} + 10H^+ \leftrightarrow 5Ca^{2+} + 6SiO_{2(aq)} \quad (16)$$

The saturation index for tobermorite is,

$$SI_{CCSH} = \log \frac{\{Ca^{2+}\}^5 \{SiO_{2(aq)}\}^6}{\{H^+\}^{10} K_{sp,CCSH}} \quad (17)$$

In the model, dissolution occurs when $SI_{CCSH} < 0$ to achieve equilibrium or until no tobermorite is present. Precipitation occurs when $SI_{CCSH} > 0$ to achieve equilibrium, and was solved numerically using the bisection method (Burden *et al.*, 2016).

Aqueous speciation. Table 1 includes all modeled aqueous speciation reactions along with their equilibrium constants and database sources. These species include H^+, OH^-, $H_2CO_{3(aq)}$, HCO_3^-, CO_3^{2-}, $SiO_{2(aq)}$, Na^+, and Ca^{2+}. Activity coefficients of all species were calculated using the Davies equation. CO_2 was modeled as an aqueous solute, not as a separate phase. The concentration of dissolved CO_2 was calculated using equations of state from Sterner and Pitzer (1994) and the solubility equations of Duan and Sun (2003). Speciation is calculated to satisfy the thermodynamic equilibrium of each species, listed in Table 1, and to satisfy the conservation of charge using the bisection method:

$$2[Ca^{2+}] + [Na^+] + [H^+] = [HCO_3^-] + 2[CO_3^{2-}] + [OH^-] \quad (18)$$

Transport

Diffusion. The governing equation for mass transport coupled with chemical reaction is as follows:

$$\frac{\partial(C_i \varphi_{d,x})}{\partial t} = D \frac{\partial}{\partial x}\left(\frac{\partial C_i}{\partial x} \varphi_{d,x}\right) + R \quad (19)$$

where C_i is the concentration of species i, t is time, D is the diffusion coefficient, $\varphi_{d,x}$ is porosity available for diffusion, x is the spatial dimension, and R is the reaction term. The equation was discretized with a forward time-centered space scheme. Diffusion coefficients were calculated depending on temperature (Supplementary Table S1). The diffusion solver and the geochemical solver were verified numerically and separately from each other.

Porosity and microporosity. Porosity available for diffusion ($\varphi_{d,x}$) in each cell was calculated based on the volumes occupied by each mineral phase and the available microporosity according to the following equation:

$$\varphi_{d,x} = 1 - V_{sand,x} - V_{CaSiO3,x} - V_{CaCO3,x} - V_{SiO2(am),x} - V_{CCSH,x} + \varphi_{\mu,x} \quad (20)$$

where $V_{i,x}$ is the volume fraction filled by i solid based on its molar volume (Table 1). The value for $V_{sand,x}$ (Fig. 2) was estimated by comparison with Plattenberger *et al.* (2019) from their column dimensions and the mass of water that could fill the pore space before injection of $CaSiO_3$. The microporosity ($\varphi_{\mu,x}$) represents the volume fraction of micron sized pore space that exists within precipitated solids. In the model, we assign the microporosity to be readily available for diffusion, but not for further precipitation. Extensive microporosity exists in layered calcium silicates (Richardson, 2008; Bonnaud *et al.*, 2012; Plattenberger *et al.*, 2019). To quantify this in the model, for the volume fraction of tobermorite present in a cell, the same volume fraction of microporosity would form according to the following equation:

$$\varphi_{\mu,x} = V_{CCSH} \quad (21)$$

In order for microporosity to limit further precipitation in a cell, the porosity available for precipitation ($\varphi_{\mu,P}$) was calculated as follows:

$$\varphi_{P,x} = \varphi_{d,x} - \varphi_{\mu,x} \tag{22}$$

Once $\varphi_{P,x}$ reaches 0, the pore space is no longer available for precipitation in that cell until one of the solid phases dissolves. We also refer to $\varphi_{P,x}$ as macroporosity.

This method of incorporating microporosity in the model provides a way to simulate continued reactive transport downstream from regions where reaction has stopped because there is no volume remaining for mineral precipitation.

Permeability

The permeability change that resulted from the mineral precipitation filling the pore space was calculated using the power law relation with porosity change:

$$\frac{k_x}{k_0} = \left(\frac{\varphi_{d,x}}{\varphi_{d,x,0}}\right)^{\alpha} \tag{23}$$

where k_x is the permeability of cell x(mD) and $\varphi_{d,x}$ is the porosity of cell x. The value k_0 is the initial permeability (mD) for each cell. The value used for the constant α was 5, within the range of values found appropriate for geologic subsurface CO_2 reservoirs (Nogues *et al.,* 2013).

The initial permeability was calculated using the Kozeny-Carman relationship:

$$k_0 = \frac{\varphi_0^3}{36c(1-\varphi_0)^2} g^2 \tag{24}$$

where φ_0 is the initial porosity available for diffusion, c is a scaling constant for the rock type, which is ~5.7 for sandstones (Rose and Bruce, 1949), and g is grain size (μm). To compare with experimental work by Plattenberger *et al.* (2019), the grain size was estimated by taking the weighted average of a 500 μm sand particle and the average $CaSiO_3$ particle size of 10.2 μm from those experiments, weighted based on their mass fractions. This grain size remained constant across simulations.

To find the permeability (K_P) of the entire length of the porous medium, the harmonic average of the individual k_x values for each cell was calculated (Khan, 2012) as follows:

$$K_P = \frac{N}{\sum^1 / k_x} \tag{25}$$

where K_P is in mD and N is the number of cells.

Simulation Conditions and Model Parameters

Simulation conditions

The first model simulation was for calibration toward published experimental data to determine precipitation rate constants. Second, the pH was increased by adding 0.1 M NaOH to examine the effect of pH on the reaction front. The simulation was also used as validation by comparing with published experimental results from Plattenberger *et al.* (2019). A third set of simulations examined the effects of $CaSiO_3$ solubility constants and dissolution rates to understand differences between wollastonite and pseudowollastonite and their effects on mineral precipitation and permeability reduction. A fourth simulation was done for field conditions at 40°C and CO_2 pressures of 7.5 MPa (Crandell *et al.*, 2010). All simulations were allowed to run to 96 h.

Model calibration

The calibration simulation (Simulation 1) results were compared to an experimental result from Plattenberger *et al.* (2019) in which a sand column containing pseudowollastonite was reacted at 150°C with boundary condition water equilibrated with 1.1 MPa CO_2. The precipitation rate constants $k_{P,i}$ were varied to yield a precipitation front most similar to the observed precipitation front of $CaCO_3$ (Fig. 3), forming near the inlet up to ~2–3 mm. The fitted $k_{P,i}$ values are in Table 1. The $CaCO_3$ front in the calibrated model

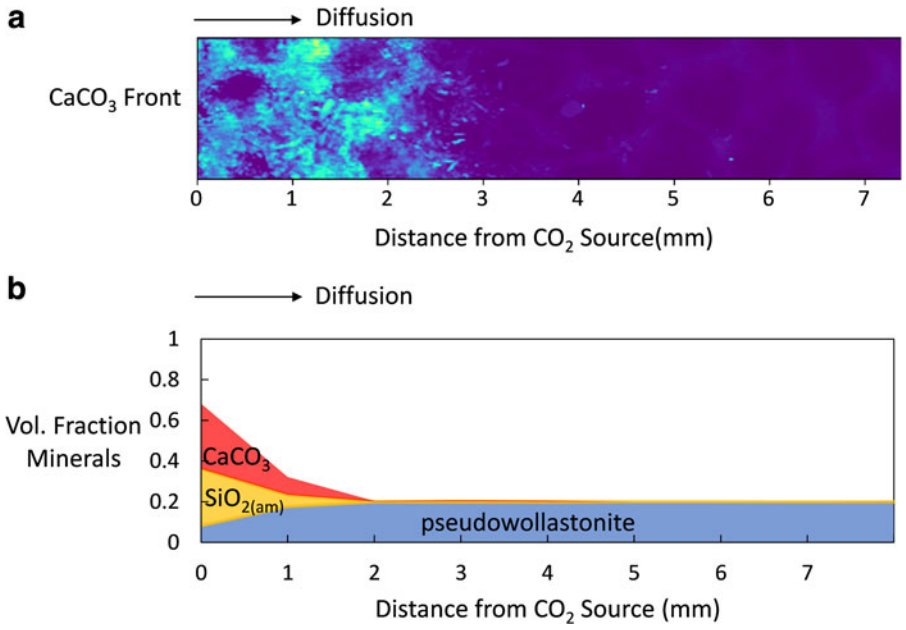

FIG. 3. **(a)** Experimental results for Simulation 1, in which pseudowollastonite in a sand column is reacted with CO_2 after 96 h. Sr had been used as an indicator for $CaCO_3$ due to its ability to coprecipitate. The XRF map shows Sr in *light blue* where $CaCO_3$ forms, and areas without Sr in *dark blue*. The carbonation front extended ~2–3 mm from the CO_2 source. **(b)** Model results for the calibration simulation show an observable amount of $CaCO_3$ in the model forming up to ~2–3 mm from the CO_2 source after 96 h. Sr, Strontium.

produced a front reaching 3 mm, although the largest amounts of $CaCO_3$ precipitation occurred nearer to the CO_2 source. Precipitation rates can vary with supersaturation, surface roughness, and particle surface area (Shiraki and Brantley, 1995; Noiriel *et al.*, 2012). The same $k_{P,i}$ values were used for the remaining simulations, despite possible variability with ionic strength, temperature, and CO_2 pressure.

Sensitivity analyses of these rate constants in pseudowollastonite reactions indicated that the $CaSiO_3$ precipitation rate constant largely controlled where the observable $CaCO_3$ precipitation front occurred (Supplementary Fig. S1a). As the rate constant $k_{P,CaSiO3}$ decreases, the amount of $CaCO_3$ near the CO_2 source at 0 mm decreases, but the amount of $CaCO_3$ farther from the CO_2 source increases. This likely occurs because rapid precipitation of $CaSiO_3$ removes Ca^{2+} from solution making it unavailable for $CaCO_3$ precipitation. Some of this Ca^{2+} is used for $CaCO_3$ formation further from the CO_2 source when $k_{P,CaSiO3}$ is lower.

The precipitation rate constant for $CaCO_3$ affects the mass of $CaCO_3$ precipitation occurring in the regions of $CaCO_3$ precipitation. As the $k_{P,CaCO3}$ increases, the rate of $CaCO_3$ precipitation increases, resulting in higher accumulation of $CaCO_3$ near the inlet at 0 mm, and lower accumulation of $CaCO_3$ at 1 mm from the inlet (Supplementary Fig. S1b).

Model validation

The model was validated in Simulation 2 as a result of adjusting the boundary pH to 6.1 by adding 0.1 M NaOH and comparing simulations with experimental results from Plattenberger *et al.* (2019). Those sand column experiments showed that, with higher pH, a small amount of $CaCO_3$ precipitation occurred at the inlet, and CCSH precipitation was predominant from the inlet to ~2–3 mm into the porous medium (Fig. 4a). The remainder of the porous medium stayed in its initial pseudowollastonite phase by 96 h of reaction, although permeability continued to decrease for 495 h. Similarly, the model showed that increased pH resulted in precipitation of $CaCO_3$ and $SiO_{2(am)}$ largely within 1 mm from the CO_2 source. A region of tobermorite precipitation formed farther in, occurring from 1 to 25 mm from the inlet by 96 h (Fig. 4b), producing more extensive CCSH precipitation than Plattenberger *et al.* (2019). This difference can be attributed to simplifications made in the model regarding CCSH formation.

Simplifications in the model were made due to the complexity of CCSH forming in experiments. Many calcium silicate hydrates like tobermorite can exist as metastable solids intergrown with each other and with a range of molar volumes depending on the amount of water molecules held within its structure (Richardson, 2008; Houston *et al.*, 2009). This model does not evaluate the effects of hydration on permeability, or the diversity of calcium silicate hydrates that can coexist in the same environment to similarly alter flow. Furthermore, the rate of tobermorite precipitation was not modeled due to the lack of known kinetic information regarding CCSH. Despite these differences, the simulated results still match at least the spatial regimes reasonably well, if not the actual length scales of those regimes.

Experimental Methods

Reactive diffusion column experiments

Glass beads (595–841 μm; Mo-Sci Corporation) were placed in a stainless steel tube (outder diameter: ¼ ,'' Wall

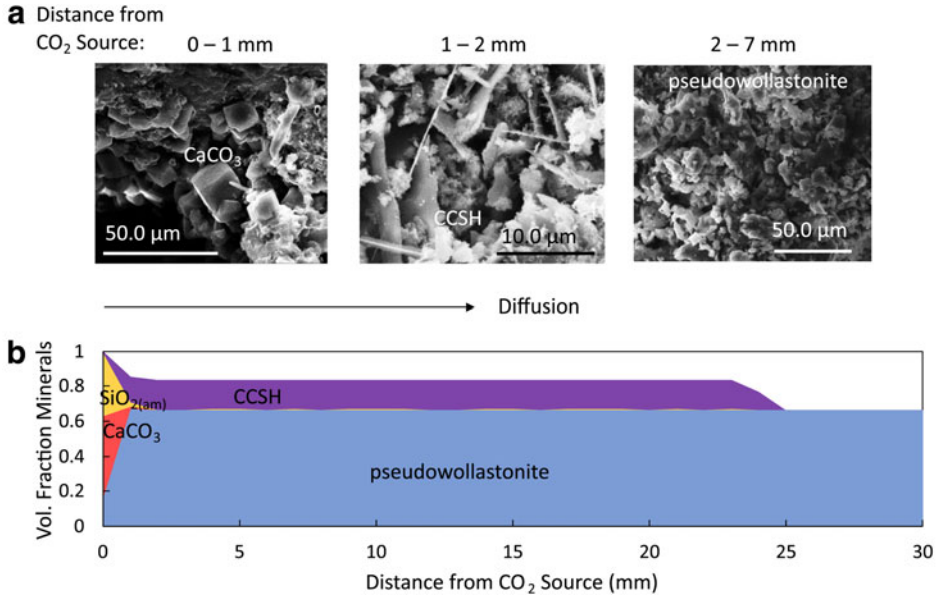

FIG. 4. **(a)** Scanning electron microscopy images of three column regimes from sand column experiments with pseudowollastonite reacted for 96 h with boundary pH 6.1. Near the CO_2 source, large distinct crystals of $CaCO_3$ were found along with low amounts of CCSH and $SiO_{2(am)}$. Around 2 mm beyond the inlet, significant amounts of plate-like crystals of CCSH were observed. The remainder of the column remained mostly unreacted pseudowollastonite. **(b)** Model simulations under the same conditions (Simulation 2) similarly produced three regimes, with $CaCO_3$ and $SiO_{2(am)}$ nearest to the CO_2 source, followed by a second regime of tobermorite (CCSH), and a third, mostly unreacted regime of $CaSiO_3$. Microporosity formed in regions where CCSH was present, while the remaining unfilled volume consisted of macropores. CCSH, crystalline calcium silicate hydrate.

thickness: 0.049,'' Length: 1'') and sintered together at 680°C following methods by Berge *et al.* (1995). A filter was placed at the outlet of the column and pseudowollastonite (Sigma-Aldrich) was flowed through the glass bead column by pressurized water to fill the pore space. The filter was then removed, and the column was allowed to dry at 105°C for 24 h. The glass bead column was then placed in a stainless steel pressure vessel (300 mL; Parr) and filled with 250 mL of deionized water. It was reacted at 120°C degrees with a CO_2 overhead pressure of 15 MPa, and allowed to react for 96 h. After reaction, the column was again dried at 105°C for 24 h. Permeability of the glass bead columns was measured before and after reaction with CO_2 using air permeability, which measures the flow rate and pressure potential of air in the column (Tanikawa and Shimamoto, 2009).

Analysis of the column and reacted solids

After removal of the steel casing, the entire reacted glass bead column was imaged with xCT using a Zeiss Xradia 520 Versa High-resolution three-dimensional (3D) X-ray tomography microscopy (Princeton Imaging and Analysis Center) with a spatial resolution of 7.5 μm. Radiographs were collected by energy 80 kV with exposure times of 8.0 s. Three-dimensional image reconstructions were carried out in Scout-and-Scan Control System Reconstructor on 2048 radiographs taken over 180 degrees. Image processing for phase segmentation was conducted using Avizo 9 (FEI Systems) software. Subvolumes ($1074 \times 1277 \times 1756$ pixels) removing curved edges of the glass bead cylinder were used for further analysis.

X-ray diffraction (PANalytical X-Pert Pro Multipurpose Diffractor, Cu-Kα) was used to analyze the $CaSiO_3$ before and after reaction with CO_2. Scanning electron microscopy (SEM) coupled with energy dispersive X-ray spectroscopy (EDS) (Quanta-650) was used to examine morphology and elemental abundance of the prereaction and postreaction materials. For SEM/EDS analysis, samples were coated with Au/Pd.

Results and Discussion

Effect of pH on calcium silicate hydrate precipitation

As expected, experiments indicate that increasing pH can cause more CCSH precipitation (Simulations 1, 2; Figs. 3 and 4), but our model reveals why this occurred by examining the concentrations of aqueous species and the coinciding precipitation over time. Mineral solubility, CO_2 solubility, and carbonate speciation all play a role.

Two boundary pH conditions of 3.5 (Fig. 3) and 6.1 (Fig. 4) were examined by maintaining an overhead pressure of 1.1 MPa CO_2 and adding 0.1 M NaOH to increase pH. The increase in pH increased the solubility of CO_2, increasing the total carbon concentration in solution at the boundary from 0.058 to 0.156 M (Fig. 5a, b), thereby increasing the amount of diffusing CO_3^{2-}. Subsequently, because $CaCO_3$ formation [Eq. (7)] is generally limited by the CO_3^{2-} supply in the system, the simulations at increased pH had more rapid $CaCO_3$ precipitation within the first 48 h (Fig. 5c, d). $CaCO_3$ precipitation began to slow near the CO_2 source in simulations at increased pH after $\sim$48 h due to limited supply of CO_3^{2-}, although minor $CaCO_3$ precipitation continued up to 85 h (Fig. 5c).

As shown in Fig. 6a, after $\sim$94 h, Ca^{2+} began to significantly accumulate near the inlet. The accumulation of Ca^{2+} over time promoted tobermorite precipitation through its influence on the saturation index (Fig. 6b). Precipitation of tobermorite occurred by 95 h (Fig. 6c) when it became oversaturated based on the SI_{CCSH}.

Increased Ca^{2+} concentration from accumulation increased SI_{CCSH}. In addition, increasing Ca^{2+} also increased pH. Based on the conservation of charge [Eq. (18)], if Ca^{2+} concentration increases, then H^+ concentration needs to decrease to maintain net neutrality for the solution, and the OH^- concentration should increase to satisfy the equilibrium for the dissociation of water (Table 1). The decrease in H^+ concentration results in further increase of SI_{CCSH} according to Equation (17). The effect of Ca^{2+} accumulation on H^+, OH^-, and the SI_{CCSH} is shown in Fig. 6d.

Spatial distribution of precipitating solids

The spatial distribution of solids throughout the porous medium in experiments with the boundary pH 6.1 can be explained by the order of reactions described above in Effect of pH on Calcium Silicate Hydrate Precipitation section. In the first regime reaching 1 mm from the inlet, $CaCO_3$ and $SiO_{2(am)}$ dominate (Fig. 4). Because $CaCO_3$ begins precipitating within the first hour of reaction and is limited by the supply of CO_3^{2-}, it forms near the CO_2 source. $SiO_{2(am)}$ precipitation, which depends on the supply of $SiO_{2(aq)}$ ions, forms where $SiO_{2(aq)}$ is released from $CaSiO_3$ dissolution, coinciding with where $CaCO_3$ forms. We note that although dissolution of $CaCO_3$ and $SiO_{2(am)}$ was included in the model, their dissolution did not play a role in our simulations due to the presence of supersaturated solutions. During the first 94 h of reaction, tobermorite remains undersaturated (Fig. 6b) and does not compete for ions near the inlet.

In the second regime from 1 to 25 mm from the inlet, tobermorite dominates by 96 h (Fig. 4). Because tobermorite precipitation depends on Ca^{2+}, $SiO_{2(aq)}$, and H^+ concentrations as opposed to CO_3^{2-} concentrations, it forms where Ca^{2+} accumulates after $CaCO_3$ precipitation has slowed, occurring after 94 h. Note that this compares well with experiments by Plattenberger *et al.* (2019), which found that permeability differences between experiments with and without NaOH did not occur until after 96 h.

In the model, tobermorite's instantaneous precipitation to reach equilibrium removes Ca^{2+} and $SiO_{2(aq)}$ ions from solution, which could be available for $CaCO_3$ and $SiO_{2(am)}$ formation. In the second regime, once $CaCO_3$ and $SiO_{2(am)}$ do become supersaturated, they are still modeled as rate-controlled precipitation reactions competing with the instantaneous, equilibrium-driven tobermorite precipitation. Although the high-volume fractions of tobermorite are partly an artifact of the different methods used to model $CaCO_3$, $SiO_{2(am)}$, and CCSH precipitation, the correct spatial pattern reproduced in the model was similar to experimental results by Plattenberger *et al.* (2019), confirming the likelihood that CCSH formation in the second regime depletes ions for $CaCO_3$ and $SiO_{2(am)}$ precipitation. On the other hand, the larger spatial extent of CCSH precipitation suggests that CCSH precipitation may be rate limited, like $CaCO_3$ and $SiO_{2(am)}$ precipitation.

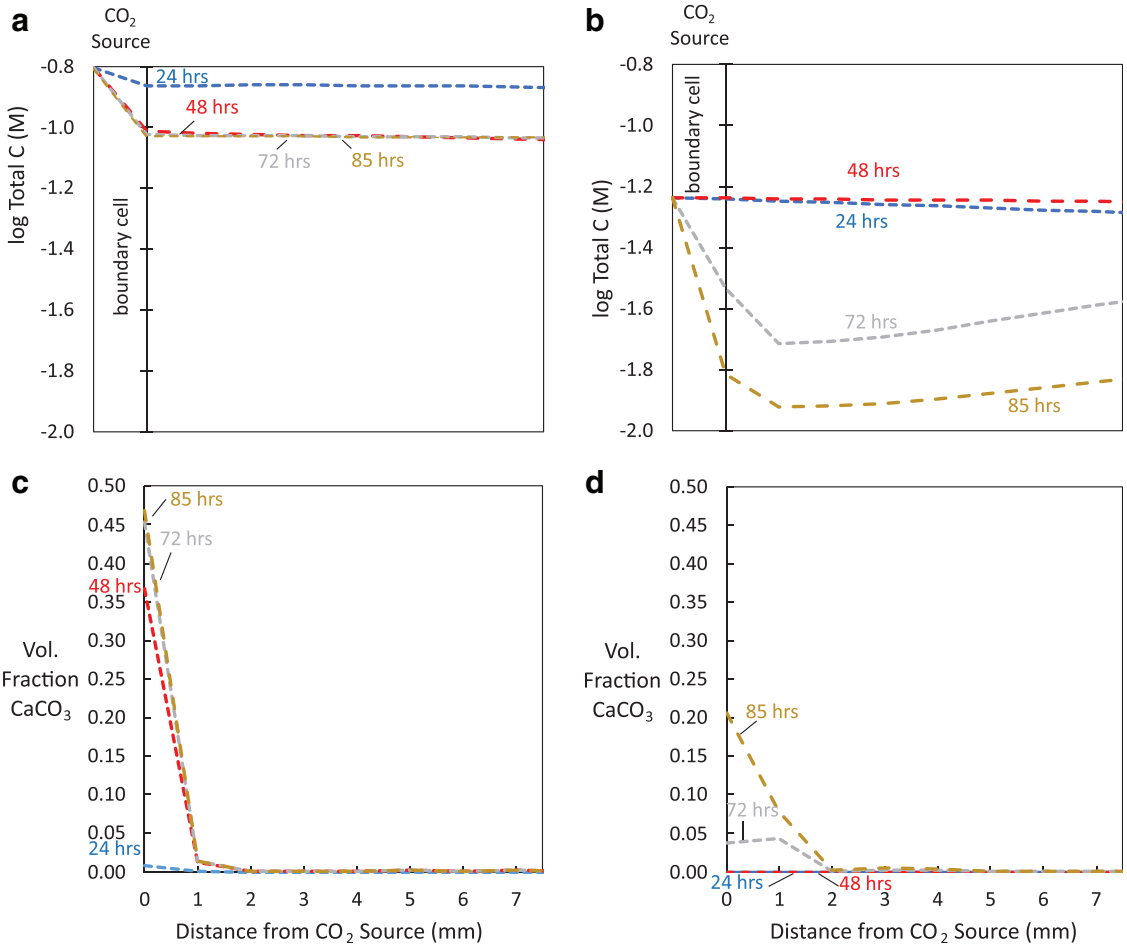

FIG. 5. In Simulation 2 with pseudowollastonite reacted with boundary pH 6.1, **(a)** the total carbon of the CO_2 source, depicted in the boundary cell and throughout the porous medium, is higher than in **(b)** the simulations with boundary pH 3.5. Consequently, $CaCO_3$ formation occurs more rapidly over time within the first 85 h and in larger amounts when **(c)** the boundary pH is 6.1 than **(d)** when the boundary pH is 3.5.

In the third regime from 25 mm to the end of the modeled porous medium (Fig. 4b), limited $CaSiO_3$ dissolution occurred with minor amounts of $CaCO_3$ formation. Although HCO_3^- and CO_3^{2-} are present in this regime, their concentrations are still less than concentrations near the inlet at 96 h, limiting $CaCO_3$ precipitation. The relatively stable pH also prevents rapid $CaSiO_3$ dissolution. Consequently, unreacted pseudowollastonite dominates the third regime.

Effects of $CaCO_3$, $SiO_{2(am)}$, and CCSH on permeability change

The predicted changes in permeability in simulations 1 and 2 coincide with accumulating precipitates and their effects on porosity. When the boundary pH is 3.5 (Simulation 1), permeability does not start to significantly decrease until after ~72 h (Fig. 7) when noticeable $CaCO_3$ and $SiO_{2(am)}$ precipitation start (Fig. 5d and Supplementary Fig. S2a). By 96 h, the simulated permeability decreases by 1 order of magnitude. Model predictions of permeability were comparable to experimental results by Plattenberger *et al.* (2019). In those experiments conducted, sand columns under the same experimental conditions decreased by 0.46 orders of magnitude in 96 h and continued to decrease by 0.84 orders of magnitude after ~168 h.

For Simulation 2 with the boundary pH 6.1, permeability starts to decrease (Fig. 7) when $CaCO_3$ and $SiO_{2(am)}$ precipitation occur from ~30 to 94 h of reaction (Figs. 5c and 3b). By 94 h, the permeability for simulated porous media decreased by ~8 orders of magnitude. After 94 h, the model shows that permeability remains relatively stable, coinciding with rapid tobermorite precipitation (Fig. 6c). Although one might expect large amounts of CCSH precipitation to decrease permeability, an explanation lies in the modeling of microporosity and its effect on permeability. In the model, microporosity is available for diffusion, but not for precipitation. However, microporosity is incorporated into the calculation of the porosity available for diffusion, $\varphi_{d,x}$, and $\varphi_{d,x}$ is used to calculate permeability. If microporosity is not used in the calculation of $\varphi_{d,x}$ for permeability, the permeability of the porous medium at 96 h lowers by an additional ~1.5 orders of magnitude from 2.96×10^{-6} to 7.04×10^{-8} mD, yielding a total permeability decrease of ~9.5 orders of magnitude. When comparing model results to experiments by Plattenberger *et al.* (2019), the modeled permeability decrease of ~8 to 9.5 orders of magnitude was less than experimentally measured permeability change. By 96 h, sand column experiments that had been reacted under the same conditions decreased by 0.75

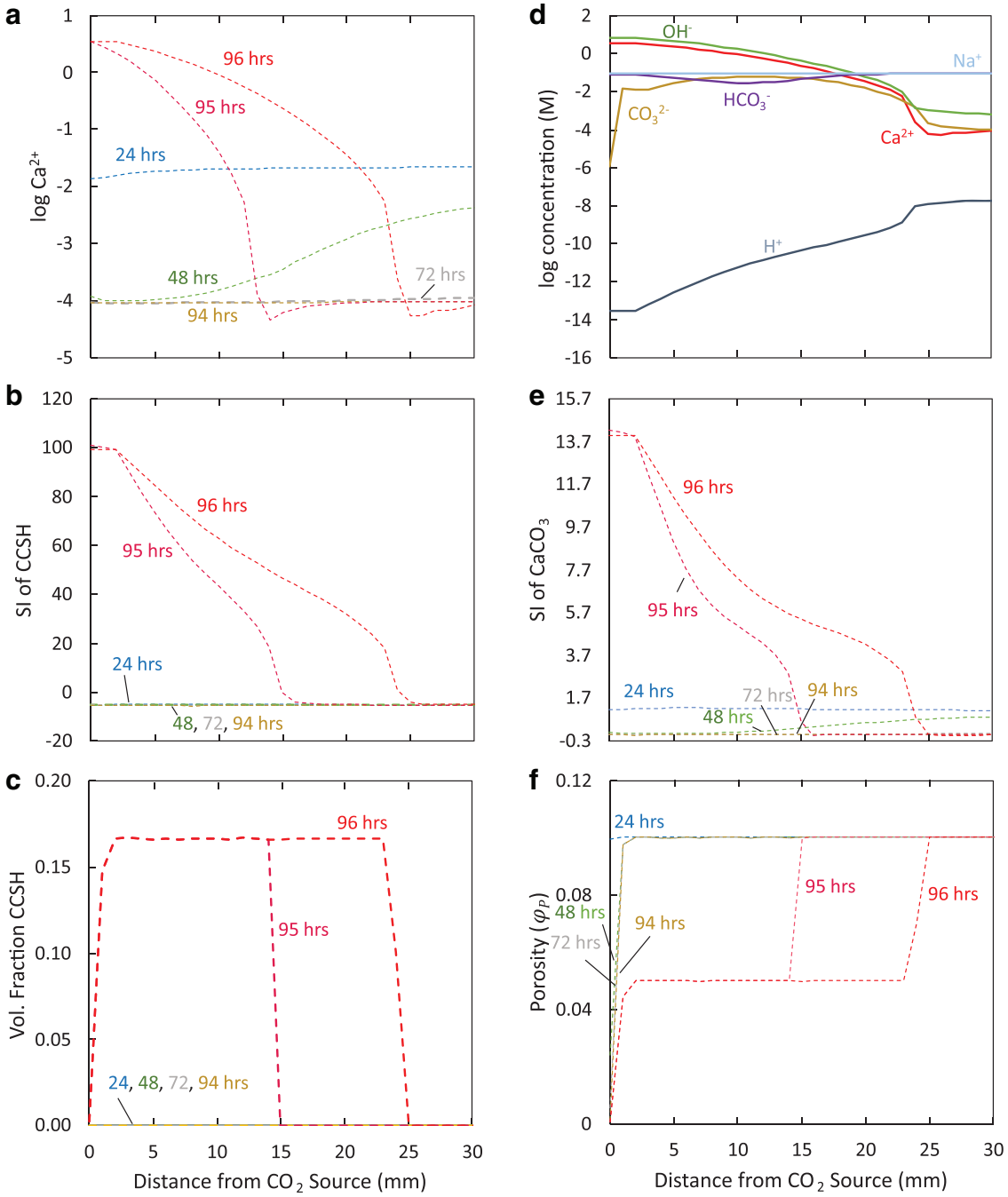

FIG. 6. In Simulation 2 with pseudowollastonite reacting with boundary pH 6.1, **(a)** Ca^{2+} accumulates significantly after 94 h when $CaCO_3$ precipitation has slowed. This, in part, increases the **(b)** SI_{CCSH}, resulting in **(c)** tobermorite precipitation to equilibrium. **(d)** At 96 h, the effect of Ca^{2+} on H^+ and OH^- concentration to achieve charge neutrality throughout the porous medium leads to decreased H^+, which also increases SI_{CCSH}. **(e)** Increased Ca^{2+} also causes supersaturation of $CaCO_3$. The formation of CCSH leads to **(f)** significant decreases in the porosity available for precipitation in the last 2 h of the simulation.

orders of magnitude. By 495 h, the permeability continued to decrease by 2.83 orders of magnitude. The complicating effects of modeling microporosity will be discussed in the following section.

The role of microporosity

The modeling of microporosity opens new doors and generates new questions. First, the inclusion of microporosity with CCSH precipitation permits continued diffusion and reaction in the model over longer time scales. In particular, for Simulation 2 with pseudowollastonite reacting with CO_2 for the case of boundary pH 6.1 (Fig. 4), the pore space available for precipitation, φ_P, decreased to 0 by 95 h of reaction at the inlet (0 mm), preventing further formation of solids at 0 mm until dissolution had occurred. Because the pore space available for diffusion, φ_d, remained greater than 0, CO_2 was able to continue diffusing through the porous

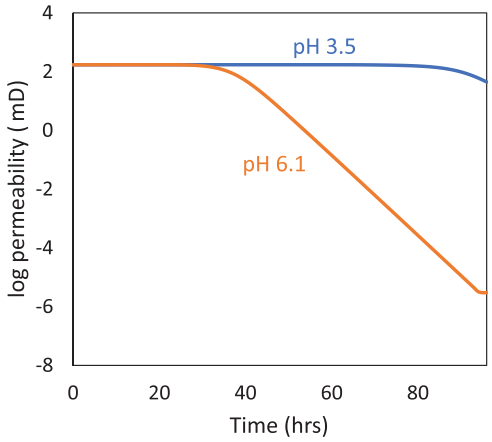

FIG. 7. Permeability decreased for simulations with pseudowollastonite reacted with CO_2 for boundary pH 3.5 (Simulation 1) and 6.1 (Simulation 2), with a larger decrease occurring at higher pH.

medium. As a result, continued precipitation of CCSH, $CaCO_3$, and $SiO_{2(am)}$ occurred after 95 h, accumulating deep into the length of porous medium. We speculate that this may be appropriate due to other studies that have found decreasing pore space inhibits the nucleation process (Putnis, 2015; Prasianakis *et al.*, 2017).

Microporosity plays an important role in filling pore space with mineral precipitation, although questions regarding its effect on permeability remain. Because microporosity represents pore space available for diffusion, it was included in the calculation of permeability. The designated amount of microporosity produced by CCSH formation, one in which the volume of micropores is equivalent to the volume of CCSH, resulted in no permeability decrease directly caused by CCSH precipitation. Despite this simulated result, we suspect that the formation of CCSH does, in fact, lead to permeability decrease, based on continued permeability decreases in sand column experiments by Plattenberger *et al.* (2019) when substantial CCSH formed. A decreased volume of microporosity resulting from CCSH formation would yield lower permeability. An improved estimation of the volume of microporosity produced from the different precipitation reactions would provide a better estimate of the actual effect of microporosity on permeability.

In addition, the model does not include microporosity from $CaCO_3$, $SiO_{2(am)}$, or $CaSiO_3$. This may account for the larger decrease in permeability in our simulations than the values measured in experiments, although the relative changes in permeability for different experiments remain accurate. We note that, in general, the effect of microporosity on permeability is poorly understood and is further complicated by pore connectivity, pore geometry, and ratio relative to macropores (Weger *et al.*, 2009; Mehmani and Prodanović, 2014; Apourvari and Arns, 2016). Nonetheless, the model provides interesting insight into how microporosity from CCSH precipitation might influence permeability.

Permeability, porosity, and pore connectivity

To better understand the role of precipitation on porosity and permeability, experiments were conducted using sintered glass bead columns containing $CaSiO_3$ to react with CO_2. The use of sintered glass beads allowed for xCT analysis and differentiation between the glass beads, pores, and minerals. Because the glass beads were sintered together, the steel casing, which would have made it difficult to differentiate between materials like $CaSiO_3$ and $CaCO_3$ that may have more similar densities, could be removed. On the other hand, the glass bead surfaces were found to undergo minor dissolution, likely releasing additional ions in solution. Due to the resulting uncertainties and complications, we did not directly model glass bead column experiments.

The xCT images of glass bead column experiments showed that material filling the pore space near the column inlet had a different density than material filling the pore space near the closed end of the column (Fig. 8a). X-ray diffraction informed by chemical compositions detected from SEM/EDS analyses indicated that calcite formed at the inlet, while the calcium silicate hydrate fedorite formed in the remaining column.

Analysis of the pore spaces showed that pore connectivity greatly decreased after $CaSiO_3$ was added and reacted with CO_2 (Fig. 8b), resulting in a permeability change of 2 orders of magnitude from 256 ± 29 to 7 ± 2 mD after 96 h of reaction. The pore connectivity arises from the 3D nature of a porous system and cannot be accounted for in a 1D model. However, the role of pore connectivity in permeability change should not be overlooked.

Comparison between wollastonite and pseudowollastonite in a diffusive system

To understand differences between wollastonite and pseudowollastonite dissolution on mineral precipitation, we modeled the effects of their distinct solubility constant, differences in dissolution rates for the two $CaSiO_3$ minerals, and differences in precipitating $CaCO_3$ mineral solubility constants.

In contrast to Simulation 2 for the 96-h simulations of pseudowollastonite reactions with CO_2 for the case of boundary pH 6.1, reactions using the wollastonite solubility constant and a slowed dissolution rate led to no tobermorite formation (Fig. 9a). The use of calcite or aragonite's solubility constant for the $CaCO_3$ phase did not affect tobermorite formation. The precipitation from $CaCO_3$ and $SiO_{2(am)}$ led to decreases in permeability by 96 h (Fig. 9b), with the change larger than the simulations for pseudowollastonite reacting with CO_2 for the case of the pH 3.5 boundary, but less than the simulations with the pH 6.1 boundary (Fig. 7).

Examination of all three parameters that varied between wollastonite and pseudowollastonite simulations, which include the $K_{sp,\,CaSiO3}$, the dissolution rate, and the $K_{sp,\,CaCO3}$, indicated that both the $K_{sp,\,CaSiO3}$ of pseudowollastonite and the more rapid pseudowollastonite dissolution rate are necessary for tobermorite formation. The difference in solubility constants, with pseudowollastonite having a higher solubility than wollastonite, allowed for more Ca^{2+} and $SiO_{2(aq)}$ to be released into solution upon $CaSiO_3$ dissolution. Similarly, the increased dissolution rate of pseudowollastonite released more Ca^{2+} and $SiO_{2(aq)}$ into solution faster than the wollastonite simulations. With increased Ca^{2+} in solution, the H^+ concentration should also decrease to satisfy the conservation of charge [Eq. (18)]. The combined effects of increased Ca^{2+}, $SiO_{2(aq)}$, and decreased H^+ led to oversaturation of

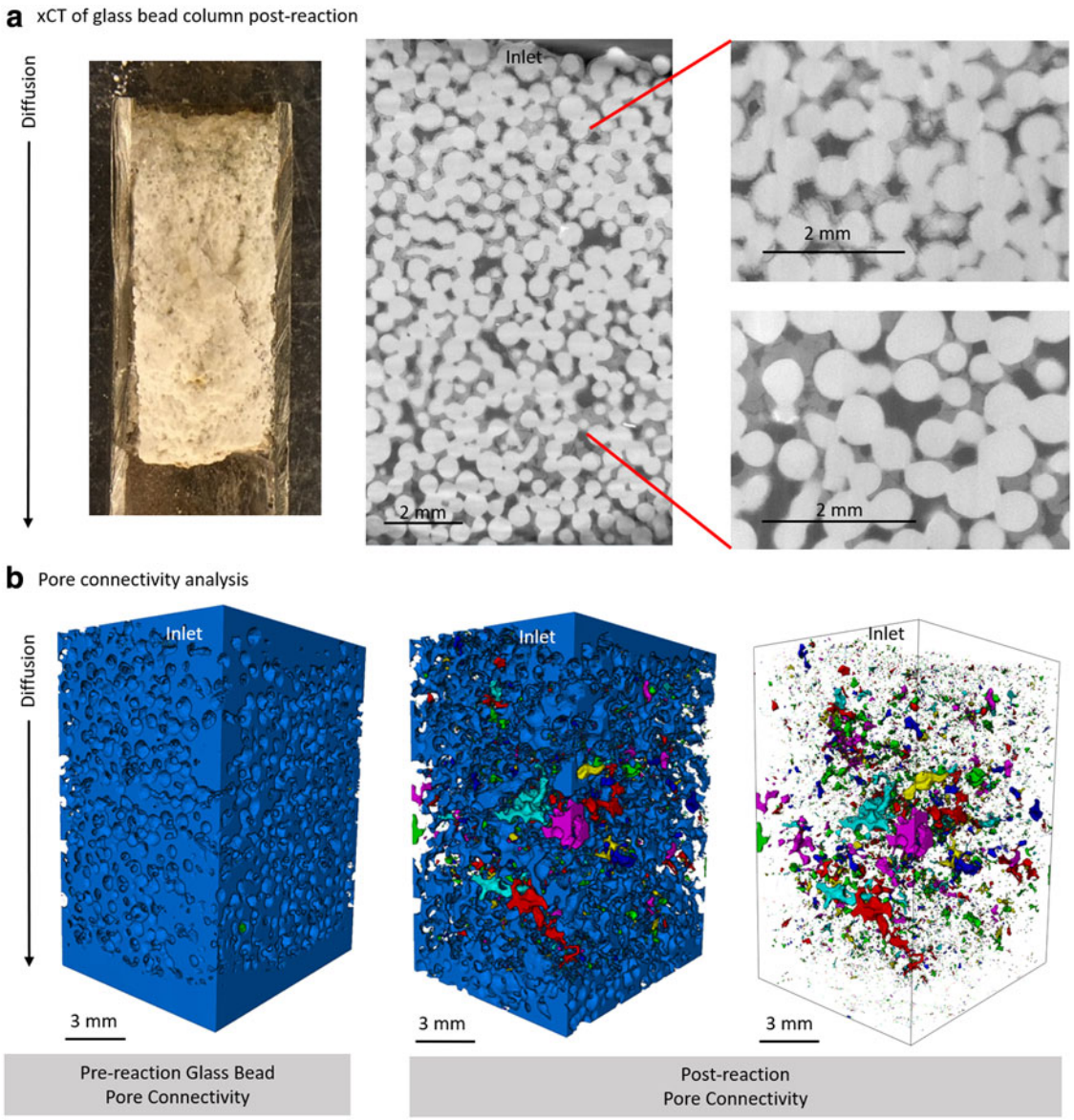

FIG. 8. **(a)** xCT of reacted pseudowollastonite in glass bead columns showed different densities in the material filling the columns near the inlet and outlet. **(b)** An analysis of which pore spaces were connected, with each color representing a separate region disconnected from the main pore network, showed that pore connectivity decreased from the addition and reaction of $CaSiO_3$. xCT, x-ray computed tomography.

tobermorite according to [Eq. (17)] in certain regions of the porous medium for pseudowollastonite simulations.

The differences in precipitation products formed from wollastonite or pseudowollastonite highlight the importance of crystal structure in predicting reactions in the field if either $CaSiO_3$ was used to seal leakages from geologic CO_2 reservoirs. Pseudowollastonite has a structure consisting of isolated trisilicate rings (Yang and Prewitt, 1999), while wollastonite consists of silicate chains (Seryotkin *et al.*, 2012). When reacting with CO_2, wollastonite dissolves nonstoichiometrically, while pseudowollastonite dissolves stoichiometrically (Casey *et al.*, 1993; Schott *et al.*, 2012). The type of dissolution has been attributed to the difference in precipitates formed between the two calcium silicates, although this work suggests that dissolution rate and solubility likely play important roles as well.

Extrapolation to field conditions for a geologic CO_2 reservoir

To examine the reactions relevant to a $CaSiO_3$-CO_2 system in a geologic CO_2 reservoir, the field conditions of 40°C and 7.5 MPa CO_2 were selected to run in the 1D model for Simulation 4. Although the boundary pH was 3.1, CCSH still formed throughout the porous medium, mostly from 1 to 44 mm at the closed end of the porous medium (Fig. 10a). In these regions, CCSH precipitates immediately at the start of the simulation. This results from the initial equilibration of pseudowollastonite throughout the porous medium at 0 h, which creates the conditions appropriate for CCSH to become supersaturated (Supplementary Fig. S3a).

The change in initial conditions at 40°C field conditions and 150°C experimental conditions results from changes in

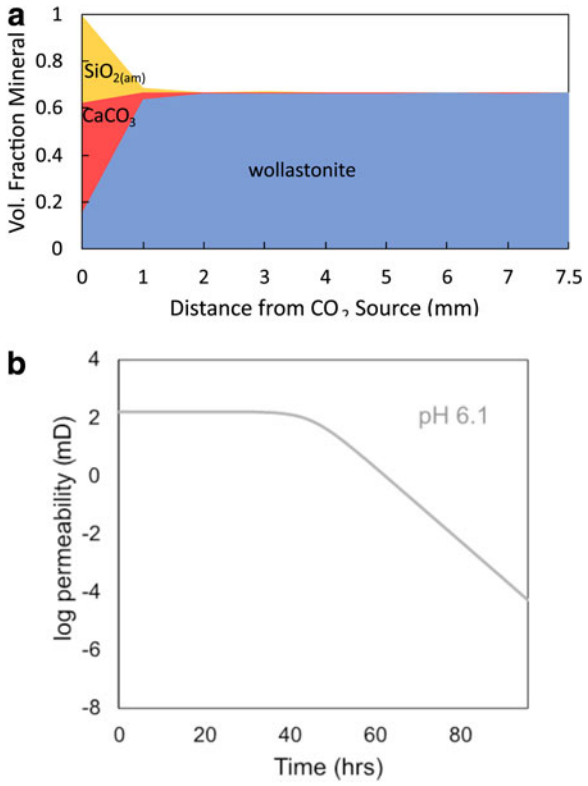

FIG. 9. Simulation 3 with the pH 6.1 boundary using the K_{sp} of wollastonite, the dissolution rate of wollastonite, and the K_{sp} of calcite as opposed to aragonite for the precipitation $CaCO_3$ produced, **(a)** $CaCO_3$ and $SiO_{2(am)}$ near the CO_2 source with no CCSH throughout the porous medium. **(b)** Permeability decreased as a result of the precipitating products.

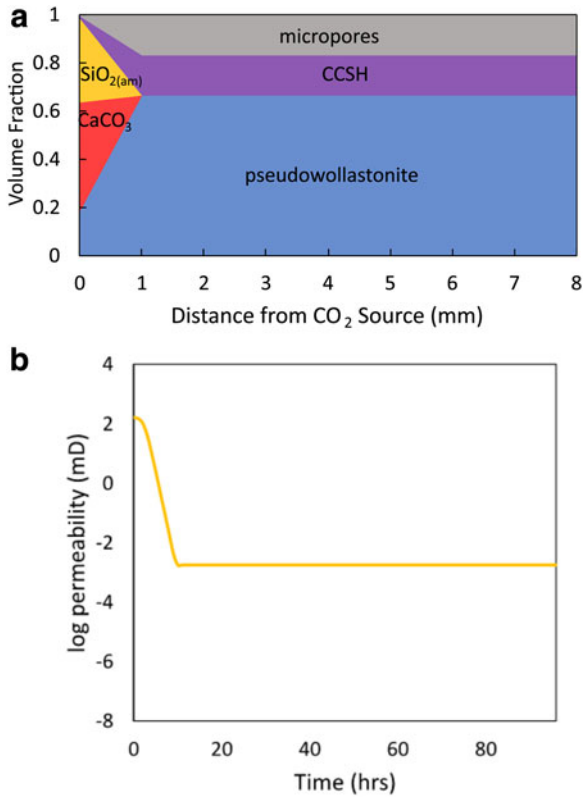

FIG. 10. Simulation 4 under field conditions at 40°C and 7.5 MPa CO_2 with no additional ions added formed **(a)** $CaCO_3$ and $SiO_{2(am)}$ near the CO_2 source along with CCSH throughout the porous medium. **(b)** Permeability decreased initially from significant CCSH formation, followed by continued decrease due to $CaCO_3$ and $SiO_{2(am)}$ precipitation until conditions became relatively stable.

equilibrium constant values due to temperature. Although the $K_{sp,CCSH}$ of tobermorite is higher at 40°C than at 150°C (Table 1), which should make tobermorite precipitation more difficult at 40°C, the change in the K_{H2O} with temperature (Table 1) and its influence on H^+ and OH^- concentration have an even larger effect on tobermorite saturation. K_{H2O} is lower at 40°C than at 150°C, yielding less dissociated H_2O at 40°C, and subsequently less H^+ and OH^-. A comparison of initial conditions at the two temperatures indicates that the initial pH throughout the porous medium at 0 h is 10.3 at 40°C, while the initial pH for the 150°C simulations is 8.1 (Supplementary Fig. S3). The significant effect of pH on SI_{CCSH} [Eq. (17)], one that exceeds those of Ca^{2+} and $SiO_{2(aq)}$, results in tobermorite precipitation at 40°C at the start of the simulation. We also note that limited CCSH formed at the inlet (0mm) due to competition with $CaCO_3$ and $SiO_{2(am)}$. The initial formation of CCSH (Supplementary Fig. S4a) is largely responsible for the rapid decrease in permeability by 1 h of reaction (Fig. 10b).

The remaining significant decreases in permeability up to 11 h result from $CaCO_3$ and $SiO_{2(am)}$ precipitation. Under field conditions, almost all $CaCO_3$ and $SiO_{2(am)}$ formation occurred rapidly within 11 h of reaction (Supplementary Fig. S4b, c). Only minor increases in precipitation and decreases in permeability continued to occur due to <0.001 vol. fraction of $CaCO_3$ precipitation at the inlet from 11 to 96 h.

The fast approach to a relatively stable environment in porous media under field conditions was initially surprising, particularly because it occurred faster than in high temperature simulations. However, an understanding of CO_2 solubility explains the unexpected result. CO_2 solubility decreases with increasing temperature. As a result, CO_2 dissolves more readily at 40°C, yielding higher total carbon concentrations for the CO_2 source than at 150°C. In addition, the field conditions had a higher overhead CO_2 pressure at 7.5 MPa, higher than the experimental overhead CO_2 pressure at 1.1 MPa. Therefore, the simulation at 150°C had total carbon concentrations of 0.05776 M for the CO_2 source, while the simulations under field conditions had total carbon concentrations of 1.152 M carbon. These increased levels of CO_2 in solution led to faster precipitation reactions for all solid phases and a faster approach to equilibrium under field conditions in comparison to the simulated conditions at 150°C.

At the same time, we recognize the limitations of the model in correctly predicting expected results under field conditions. In particular, the precipitation rate constants for $CaSiO_3$, $CaCO_3$, and $SiO_{2(am)}$ were calibrated to match with the $CaCO_3$ precipitation front produced in experiments at 150°C. These rate constants may change with temperature, but due to the complexity of precipitation rates, we chose to keep them constant across all simulations.

Implications

These modeling results using field conditions typical for a geologic CO_2 reservoir yield promising insights into deploying $CaSiO_3$ particles for targeted mineral precipitation. The predicted precipitation of CCSH under field conditions has positive implications for using pseudowollastonite for targeted mineral precipitation. CCSH formation will likely contribute to significant decreases in porosity and permeability, particularly considering the large molar volumes of different CCSH phases in comparison to aragonite and calcite.

The expected formation of CCSH under field conditions may also improve the long-term stability of precipitated minerals used to prevent further leakage of CO_2 or other subsurface contaminants. The observed acid resistivity of certain CCSH relative to $CaCO_3$ will likely prove useful. The spatial relationship between $CaCO_3$ and CCSH precipitation also results in the advantageous formation of a thicker precipitation barrier that would not be possible with only $CaCO_3$ formation. $CaCO_3$ formation relies largely on the supply of CO_3^{2-}, which is heavily limited by CO_2 diffusion. In addition, the presence of CO_3^{2-} is also limited by pH, with CO_3^{2-} forming as the dominant carbonate species only at high pH. Most systems may not reach a high enough pH for CO_3^{2-} to be the dominating carbonate ion. CCSH formation, on the other hand, depends on the more abundant Ca^{2+} and $SiO_{2(aq)}$ ions, along with an alkaline pH that can arise naturally from the presence of Ca^{2+}. The formation of different regimes of precipitation resulting from diffusion-limited species emphasizes the complexity of transport in such systems, and hints at the possibility of engineering multilayered barriers for targeted mineralization.

In addition, this work elucidates the role that basic conditions may play in developing targeted mineralization technology. The presence of other ions can influence the solubility of CO_2, consequently affecting the rates of precipitation, the supply of diffusing ions, and the potential for taking advantage of multiple forms of precipitation in a mineralized barrier. The application of adding basic ions may be used for improving outcomes during the process of sealing leakages if $CaSiO_3$ nanoparticles were injected in a pH-adjusted solution. In addition to controlling injected mixtures, the presence of other ions can also affect the pH of diffusing solutions, determining the amount of dissolution and precipitation that may occur. Such considerations are relevant to leakages occurring in a wide variety of subsurface settings, including those that contain brines.

The development of this 1D model enabled us to explore the deployment of $CaSiO_3$ particles in the subsurface. We can now examine different solution conditions, a diversity of rock types, a variety of $CaSiO_3$ particle sizes, and the effects of uneven distribution of $CaSiO_3$ minerals within the porous medium depending on where they accumulate after deployment. This model will help tackle the complex systems in which targeted mineral precipitation technology will be implemented.

Acknowledgment

We thank Zhiyuan Tao for his contribution to glass bead column experiments.

Author Disclosure Statement

No competing financial interests exist.

Funding Information

This work was supported by the U.S. Department of Energy National Energy Technology Laboratory (Grant DE-FE0026583 to the University of Virginia and Grant DE-FE0026582 to Princeton University) and the National Science Foundation (Grant NSF CBET-1805075 to the University of Virginia). The authors acknowledge the use of Princeton's Imaging and Analysis Center, which is partially supported by the Princeton Center for Complex Materials through the National Science Foundation-MRSEC program (DMR-1420541).

Supplementary Material

Supplementary Table S1
Supplementary Figure S1
Supplementary Figure S2
Supplementary Figure S3
Supplementary Figure S4

References

Apourvari, S.N., and Arns, C.H. (2016). Image-based relative permeability upscaling from the pore scale. *Adv. Water Resour*. 95, 161.

Ashraf, W., and Olek, J. (2016). Carbonation behavior of hydraulic and non-hydraulic calcium silicates: Potential of utilizing low-lim calcium silicates in cement-based materials. *J. Mater. Sci.* 51, 6173.

Berge, P.A., Bonner, B.P., and Berryman, J.G. (1995). Ultrasonic velocity-porosity relationships for sandstone analogs made from fused glass beads. *Geophysics* 60, 108.

Berner, R.A., Lasaga, A.C., and Garrels, R.M. (1983). The carbonate-silicate geochemical cycle and its effect on atmospheric carbon dioxide over the past 100 million years. *Am. J. Sci*. 283, 641.

Bielicki, J.M., Peters, C.A., Fitts, J.P., and Wilson, E.J. (2015). An examination of geologic carbon sequestration policies in the context of leakage potential. *Int. J. Greenh. Gas Control* 37, 61.

Bielicki, J.M., Pollak, M.F., Deng, H., Wilson, E.J., Fitts, J.P., and Peters, C.A. (2016). The leakage risk monetization model for geologic CO_2 storage. *Environ. Sci. Technol*. 50, 4923.

Bohnhoff, M., and Zoback, M.D. (2010). Oscillation of fluid-filled cracks triggered by degassing of CO_2 due to leakage along wellbores. *J. Geophys. Res*. 115, 1.

Bonnaud, P.A., Ji, Q., Coasne, B., Pellenq, R.J.-M., and Van Vliet, K.J. (2012). Thermodynamics of water confined in porous calcium-silicate-hydrates. *Langmuir* 28, 11422.

Burden, R.L., Faires, J.D., and Burden, A.M. (2016). *Numerical Analysis* (10th ed.). Boston, MA: Cengage Learning.

Casey, W.H., Westricht, H.R., Banfield, J.F., Ferruzzi, G., and Arnold, G.W. (1993). Leaching and reconstruction at the surfaces of dissolving chain-silicate minerals. *Nature* 366, 253.

Chou, L., Garrels, R.M., and Wollast, R. (1989). Comparative study of the kinetics and mechanisms of dissolution of carbonate minerals. *Chem. Geol*. 78, 269.

Crandell, L.E., Ellis, B.R., and Peters, C.A. (2010). Dissolution potential of SO2 Co-injected with CO_2 in geologic sequestration. *Environ. Sci. Technol*. 44, 349.

Daval, D., Martinez, I., Corvisier, J., Findling, N., Goffé, B., and Guyot, F. (2009a). Carbonation of Ca-bearing silicates, the case of wollastonite: Experimental investigations and kinetic modeling. *Chem. Geol*. 265, 63.

Daval, D., Martinez, I., Guigner, J.-M., Hellmann, R., Corvisier, J., Findling, N., Dominici, C., Goffé, B., and Guyot, F. (2009b). Mechanism of wollastonite carbonation deduced from micro- to nanometer length scale observations. *Am. Mineral*. 94, 1707.

Deng, H., Bielicki, J.M., Oppenheimer, M., Fitts, J.P., and Peters, C.A. (2017). Leakage risks of geologic CO_2 storage and the impacts on the global energy system and climate change mitigation. *Clim. Change* 144, 151.

Deng, H., Fitts, J.P., Tappero, R.V, Kim, J.J., and Peters, C.A. (2020). Acid erosion of carbonate fractures and accessibility of arsenic-bearing minerals: In Operando synchrotron-based microfluidics experiment. *Environ. Sci. Technol*. 54, 12502.

Deng, H., and Peters, C.A. (2019). Reactive transport simulation of fracture channelization and transmissivity evolution. *Environ. Eng. Sci*. 36, 90.

Dove, P.M., and Crerar, D.A. (1990). Kinetics of quartz dissolution in electrolyte solutions using a hydrothermal mixed flow reactor. *Geochim. Cosmochim. Acta* 54, 955.

Duan, Z., and Sun, R. (2003). An improved model calculating CO_2 solubility in pure water and aqueous NaCl solutions from 273 to 533 K and from 0 to 2000 bar. *Chem. Geol*. 193, 257.

Giammar, D.E., Wang, F., Guo, B., Surface, J.A., Peters, C.A., Conradi, M.S., and Hayes, S.E. (2014). Impacts of diffusive transport on carbonate mineral formation from magnesium silicate-CO_2-water reactions. *Environ. Sci. Technol*. 48, 14344.

Houston, J., Maxwell, R., and Carroll, S. (2009). Transformation of meta-stable calcium silicate hydrates to tobermorite: Reaction kinetics and molecular structure from XRD and NMR spectroscopy. *Geochem. Trans.* 10, 1.

Icenhower, J.P., and Dove, P.M. (2000). The dissolution kinetics of amorphous silica into sodium chloride solutions: Effects of temperature and ionic strength. *Geochim. Cosmochim. Acta* 64, 4193.

Jun, Y.S., Giammar, D.E., and Werth, C.J. (2013). Impacts of geochemical reactions on geologic carbon sequestration. *Environ. Sci. Technol*. 47, 3.

Khan, I.H. (2012). *Textbook of Geotechnical Engineering*. New Delhi: PHI Learning Private Limited.

Kim, D., Peters, C.A., and Lindquist, W.B. (2011). Upscaling geochemical reaction rates accompanying acidic CO_2-saturated brine flow in sandstone aquifers. *Water Resour. Res*. 47, 1.

Lee, H., Dellatore, S.M., Miller, W.M., and Messersmith, P.B. (2007). Mussel-inspired surface chemistry for multifunctional coatings. *Science* 318, 426.

Mehmani, A., and Prodanović, M. (2014). The effect of microporosity on transport properties in porous media. *Adv. Water Resour*. 63, 104.

Monasterio-Guillot, L., Di Lorenzo, F., Ruiz-Agudo, E., and Rodriguez-Navarro, C. (2019). Reaction of pseudowollastonite with carbonate-bearing fluids: Implications for CO_2 mineral sequestration. *Chem. Geol*. 524, 158.

Nogues, J.P., Fitts, J.P., Celia, M.A., and Peters, C.A. (2013). Permeability evolution due to dissolution and precipitation of carbonates using reactive transport modeling in pore networks. *Water Resour. Res*. 49, 6006.

Noiriel, C., Steefel, C.I., Yang, L., Ajo-franklin, J., Noiriel, C., and Ajo-Franklin, J. (2012). Upscaling calcium carbonate precipitation rates from pore to continuum scale. *Chem. Geol*. 318, 60.

Plattenberger, D., Brown, T., Ling, F.T., Lyu, X., Fitts, J., Peters, C.A., and Clarens, A.F. (2020). Feasibility of using reactive silicate particles with temperature-responsive coatings to enhance the security of geologic carbon storage. *Int. J. Greenh. Gas Control.* 95, 102976.

Plattenberger, D.A., Ling, F.T., Peters, C.A., and Clarens, A.F. (2019). Targeted permeability control in the subsurface via calcium silicate carbonation. *Environ. Sci. Technol*. 53, 7136.

Plattenberger, D.A., Ling, F.T., Tao, Z., Peters, C.A., and Clarens, A.F. (2018). Calcium silicate crystal structure impacts reactivity with CO_2 and precipitate chemistry. *Environ. Sci. Technol*. 5, 558.

Plummer, L.N., Wigley, T.M.L., and Parkhust, D.L. (1978). The kinetics of calcite dissolution in CO_2-water systems at 5 degrees to 60 degrees C and 0.0 to 1.0 atm CO_2. *Am. J. Sci*. 278, 179.

Prasianakis, N.I., Curti, E., Kosakowski, G., Poonoosamy, J., and Churakov, S.V. (2017). Deciphering pore-level precipitation mechanisms. *Sci. Rep*. 7, 1.

Prieto, M., Putnis, A., Fernández-Díaz, L., and López-Andrés, S. (1994). Metastability in diffusing-reacting systems. *J. Cryst. Growth* 142, 225.

Ptáček, P., Noskova, M., Brandštetr, J., Šoukal, F., and Opravil, T. (2011). Mechanism and kinetics of wollastonite fibre dissolution in the aqueous solution of acetic acid. *Powder Technol*. 206, 338.

Putnis, A. (2015). Transient porosity resulting from fluid–mineral interaction and its consequences. *Rev. Mineral. Geochem*. 80, 1.

Richardson, I.G. (2008). The calcium silicate hydrates. *Cement Concrete Res*. 38, 137.

Rose, W., and Bruce, W. (1949). Evaluation of capillary character in petroleum reservoir rock. *Pet. Trans*. 127.

Schott, J., Pokrovsky, O.S., Spalla, O., Devreuz, F., Gloter, A., and Mielczarski, J.A. (2012). Formation, growth and transformation of leached layers during silicate minerals dissolution: The example of wollastonite. *Geochim. Cosmochim. Acta* 98, 259.

Seryotkin, Y.V., Sokol, E.V., and Kokh, S.N. (2012). Natural pseudowollastonite: Crystal structure, associated minerals, and geological context. *Lithos* 134, 75.

Shiraki, R., and Brantley, S.L. (1995). Kinetics of near-equilibrium calcite precipitation at 100°C: An evaluation of elementary reaction-based and affinity-based rate laws. *Geochem. Trans*. 59, 1457.

Spokas, K., Fang, Y., Fitts, J.P., Peters, C.A., and Elsworth, D. (2019). Collapse of reacted fracture surface decreases permeability and frictional strength. *J. Geophys. Res. Solid Earth* 124, 12799.

Stack, A.G., Fernandez-Martinez, A., Allard, L.F., Bañuelos, J.L., Rother, G., Anovitz, L.M., Cole, D.R., and Waychunas, G.A. (2014). Pore-size-dependent calcium carbonate precipitation controlled by surface chemistry. *Environ. Sci. Technol*. 48, 6177.

Sterner, M., and Pitzer, K.S. (1994). An equation of state for carbon dioxide valid from zero to extreme pressures. *Contrib. Mineral. Petrol*. 117, 362.

Tanikawa, W., and Shimamoto, T. (2009). Comparison of Klinkenberg-corrected gas permeability and water permeability in sedimentary rocks. *Int. J. Rock Mech. Min. Sci*. 46, 229.

Tao, Z., Fitts, J.P., and Clarens, A.F. (2016). Feasibility of carbonation reactions to control permeability in the deep subsurface. *Environ. Eng. Sci*. 33, 778.

Weger, R.J., Eberli, G.P., Baechle, G.T., Massaferro, J.L., and Sun, Y.-F. (2009). Quantification of pore structure and its effect on sonic velocity and permeability in carbonates. *AAPG Bull*. 93, 1297.

White, S., Carroll, S., Chu, S., Bacon, D., Pawar, R., Cumming, L., Hawkins, J., Kelley, M., Demirkanli, I., Middleton, R., Sminchak, J., and Pasumarti, A. (2020). A risk-based approach to evaluating the Area of Review and leakage risks at CO_2 storage sites. *Int. J. Greenh. Gas Control* 93, 102884.

Yang, H., and Prewitt, C.T. (1999). On the crystal structure of pseudowollastonite ($CaSiO_3$). *Am. Mineral*. 84, 929.

Zhao, H., Park, Y., Lee, D.H., and Park, A.-H.A. (2013). Tuning the dissolution kinetics of wollastonite via chelating agents for CO_2 sequestration with integrated synthesis of precipitated calcium carbonates. *Phys. Chem. Chem. Phys*. 15, 15185.